Universal three-state nematicity and magneto-optical Kerr effect in the charge density waves in AV_3Sb_5 (A=Cs, Rb, K)

Yishuai Xu,[1] Zhuoliang Ni,[1] Yizhou Liu,[2] Brenden R. Ortiz,[3]
Stephen D. Wilson,[3] Binghai Yan,[2] Leon Balents,[4] and Liang Wu[1, *]

[1]*Department of Physics and Astronomy, University of Pennsylvania, Philadelphia, Pennsylvania 19104, U.S.A*
[2]*Department of Condensed Matter Physics, Weizmann Institute of Science, Rehovot, Israel*
[3]*Materials Department and California Nanosystems Institute,*
University of California Santa Barbara, Santa Barbara, California 93106, USA
[4]*Kavli Institute for Theoretical Physics, University of California,*
Santa Barbara, Santa Barbara, California 93106, USA
(Dated: September 27, 2022)

The kagome lattice provides a fascinating playground to study geometrical frustration, topology and strong correlations[1–13]. The newly discovered kagome metals AV_3Sb_5 (A=K, Rb, Cs) exhibit various interesting phenomena including topological band structure[14–18], symmetry-breaking charge density waves (CDWs)[16, 19–37] and superconductivity[14, 15, 38–41]. Nevertheless, the nature of the symmetry breaking in the CDW phase is not yet clear, despite the fact that it is crucial to understand whether the superconductivity is unconventional. In this work, we perform scanning birefringence microscopy and find that six-fold rotation symmetry is broken at the onset of the CDW transition temperature in all three compounds. Spatial imaging and angle dependence of the birefringence show a universal three nematic domains that are $120°$ to each other. We propose staggered CDW orders with a relative π phase shift between layers as a possibility to explain the three-state nematicity in AV_3Sb_5. We also perform magneto-optical Kerr effect and circular dichroism measurements on all three compounds, and the onset of the both signals is at the CDW transition temperature, indicating broken time-reversal symmetry and the existence of the long-sought loop currents in the CDW phase. Our work strongly constrains the nature of the CDWs and sheds light on possible unconventional superconductivity in AV_3Sb_5.

The kagome lattice has attracted tremendous research interest for decades as the corner sharing triangular lattice has inherent geometrical frustrations that host exotic phases such as the quantum spin liquid state [1–3]. There has been recent interest in the magnetic kagome systems from the perspective of the topological electronic structures such as the magnetic Weyl semimetals Mn_3Sn[11], $Co_3Sn_2S_2$ [42, 43] and strongly correlated flat bands in Fe_3Sn_2 and FeSn [4–10]. Strong electronic correlations without magnetism can also lead to exotic phases such as high-Tc superconductivity, but it has been often difficult to reveal different kinds of broken symmetries. Loop currents, originally proposed in cuprate superconductors [44], have also been predicted in the kagome lattice [28, 45–47], but a clear evidence has been lacking.

The newly discovered kagome metals AV_3Sb_5 (A=K, Rb, Cs) are recent examples of hosting charge density waves (CDWs) below $T_{CDW} \approx$ 80-100 K and superconductivity below $T_C \approx$ 0.9-2.5 K. Different from magnetic kagome materials, AV_3Sb_5 do not have a detectable local electronic moments [48, 49], but a surprisingly large anomalous Hall effect was reported with dominating extrinsic skew scattering mechanism[50, 51]. An increase of the muon depolarization below the CDW transition temperature in zero-field μSR measurements in KV_3Sb_5[48] and CsV_3Sb_5[49] have been interpreted as the evidence

of the time-reversal symmetry (TRS) breaking, but the onset temperature is not always at T_{CDW} and the muon depolarization is not directly related with the TRS-breaking order parameter [48, 49]. Therefore, a direct measurement of the TRS-breaking order parameter at zero-field is urgently needed. Another major debate in the community is whether the system has a six-fold or two-fold rotational symmetry in the CDW phase [20, 30, 52–56], and at what temperature the six-fold symmetry breaks. Almost all of the experiments that claimed the two-fold symmetry were performed at temperature much below the CDW transition[20, 53, 56, 57]. Therefore, whether the two-fold symmetry is directly related to the CDW has not been clear. In this work, we use scanning birefringence microscopy, magneto-optical Kerr effect, and circular dichroism to reveal that the CDW transition temperature is the onset of six-fold rotational symmetry breaking and TRS breaking. Our micron-scale imaging bridges the gap between nano-scale scanning probes and macroscopic measurements, and provides new insight and strong constrains on the interpretation of many results by macroscopic probes.

Three-state nematicity

AV_3Sb_5 (A=K, Rb, Cs) share a hexagonal crystal structure, consisting of a kagome lattice of V atoms coordinated by Sb in the V-Sb sheet stacked between the A sheets, as shown in Fig. 1(a). Therefore, it is six-fold rotationally symmetric in the normal state above T_{CDW}. In the CDW phase, the 2×2 superlattice per layer could

form the star-of-David (SoD) or the tri-hexgonal (TrH) pattern, which still keep the six-fold symmetry in the pristine lattice. Nevertheless, a π phase shift between neighboring layers can reduce the symmetry to two-fold, as as shown in Fig. 1(b) and Extended Fig. 1(a). Note that electronically-driven nematicity is also two-fold symmetric, but the onset temperature is much below T_{CDW} as observed by scanning tunnelling microscopy (STM)[20, 53, 56].

To study the rotational symmetry in the CDW phase, we perform scanning birefringence measurements as shown in Fig. 1(c). Under normal incidence, the change of the polarization, θ_T, depends not only on the out-of-plane magnetization or orbital moment, known as the magneto-optical Kerr effect (MOKE), but also on the birefringence term when the rotational symmetry is lower than three-fold. We can distinguish two contributions by rotating the polarization of the incident beam,

$$\theta_T = \theta_K + \theta_B \sin(2\phi - \phi_0) \tag{1}$$

where θ_K and θ_B represent the real part of the MOKE and the amplitude of the birefringence; ϕ is the polarization angle of the incident light with respect to the horizontal axis in the lab. ϕ_0 is one principal axis of the crystal in the lab frame. Note that the "MOKE", $\theta_K + i\eta$, is actually a complex quantity, and the θ_K and η are often called MOKE and ellipticity, respectively. (See Methods.) Fig. 1(d) shows temperature-dependent θ_T at different polarization for RbV$_3$Sb$_5$, and the onset of θ_T is at $T_{CDW} \approx 103$ K. As we change the polarization of the incident light, both the sign and the magnitude of θ_T changes with a maximum amplitude of 0.27 mRad at 6 K. Plotting the θ_T vs the incident polarization at a constant temperature shows a two-fold symmetric pattern below T_{CDW} (see Fig. 1(e)). In contrast, we barely observe any angle dependence above T_{CDW}, which is consistent with the six-fold symmetry of the kagome lattice. The two-fold symmetric pattern originates from the breaking of the six-fold rotation symmetry due to the formation of the CDW.

We set the incident polarization at a fixed polarization, and perform a mapping of θ_T with a spatial resolution of 8 μm as shown in Fig. 1(f). Three distinct domains marked with red, white and blue are clearly seen in the map. An angle dependent birefringence measurements in the selected six regions show that the regions with the same color have the same polar patterns, as shown in Fig. 1(g-i) and extended Fig.1 1(d-f). Between regions with different color, the polar patterns are rotated by approximately 120° to each other. Fig. 2 shows that KV$_3$Sb$_5$ and CsV$_3$Sb$_5$ also have three domains, where the principal axis is also rotated by 120° from each other. The temperature dependence of the birefringence of KV$_3$Sb$_5$ and CsV$_3$Sb$_5$ also shows that the onset of six-fold rotational symmetry breaking is at T_{CDW}, ≈ 74 K and ≈ 92 K for these two compounds respectively (See Extended Fig.2). To summarize, the three nematic domains are a univer-

sal feature of the CDW phases in AV$_3$Sb$_5$(A=Cs, Rb, K).

Magneto-optical Kerr effect

In Eq. (1), there is an possible isotropic term θ_K coming from the MOKE due to TRS breaking. The isotropic MOKE term appears as an offset in the θ_T vs ϕ plot (Fig.1e, Fig.2b,d and Extended Fig. 2b, d). We extract the temperature dependent MOKE term by fitting the angle dependence by Eq. 1, and the results for the three compounds are plotted in Fig. 3a-c. RbV$_3$Sb$_5$, CsV$_3$Sb$_5$, and KV$_3$Sb$_5$ show the onset of the MOKE at approximately 103 K, 92 K and 74 K, respectively. Our result agrees with another study on the Cs compound [52]. The fitting also yield one principal axis direction ϕ_0.

We use a second method to measure the MOKE with denser temperature steps by setting the incident polarization at the principal axis to eliminate the birefringence. The temperature dependent MOKE by this method for RbV$_3$Sb$_5$, CsV$_3$Sb$_5$, and KV$_3$Sb$_5$ are shown in Fig. 3d-f. They clearly show that the onset of the MOKE signal is universally at T_{CDW} for AV$_3$Sb$_5$. There is an error bar of ±0.8° in determining the principal axis, but as Extended Fig.3 shows, the temperature dependent MOKE at $\phi_0 \pm 0.8°$ still exhibit the onset of MOKE signal at T_{CDW}. Also, a simple estimate assuming that the exact zero birefringence angle is off by 0.8° gives an error bar of 3.7 μrad (sin(0.8°) × 270 μrad).

Note that the two methods in Fig. 3 are performed at different locations and different thermal cycles, which lead to the different magnitude and signs. Different MOKE signs at various regions are also consistent with two TRS breaking domains. To confirm the consistency between the two methods, we measure the MOKE signal again by the second method in region 2 of RbV$_3$Sb$_5$, and obtain similar data as method 1 as shown in Extended Fig. 1d. Furthermore, as shown in Extended Fig.4, thermal cycles at the same location can give rise to different signs of the MOKE signal, which is another strong evidence for the time-reversed domains. The contour of the birefrigence domain does not change much, but the intensity of θ_T changes a little bit perhaps due to change of the MOKE contribution. To summarize, our MOKE measurement at zero field directly probe the TRS-breaking order parameter and demonstrate that TRS is broken at the T_{CDW} for all three AV$_3$Sb$_5$ compounds, indicating the existence of the long-sought loop currents in the CDW phases in AV$_3$Sb$_5$ as shown in the inset of Fig. 3d.

Circular dichroism

To further confirm TRS breaking in the CDW phase, we measure the circular dichroism (CD) on these three compounds. Left circularly polarized (LCP) and right circularly polarized (RCP) light are normally incident on the sample, and the difference of the reflectivity between the LCP and RCP is defined as the CD. The CD measurement is free from the birefringence effect and fitting errors. The measured CD signal can be shown to be pro-

portional to the ellipticity, η, of the MOKE contribution (see Methods). Fig. 4 shows the CD vs temperature for all three compounds at different spatial locations, and we clearly see an onset of CD at T_{CDW} as the temperature-dependent CD at different spots of the samples splits at T_{CDW}. The locations of these points are shown in the the spatial CD mapping in Extended Fig.5.

Note that CD can also originate from chiral (handed) structures, and there has been theoretical proposals that the CDW on the surface of AV_3Sb_5 could be chiral if the period along the c axis is of four unit cells [45]. When the structure becomes chiral (handed), it breaks all of the mirror symmetries and, therefore, breaks the inversion symmetry. We performed second harmonic generation experiments, and observe that the SHG signal is only around 0.2 counts of photons per second under 12 mW incident power. We also do not see any change across the T_{CDW}. Our observation of AV_3Sb_5 being centrosymmetric agrees with previous studies [30, 49], and our detection sensitivity is much higher [58, 59]. Interestingly, in the CsV_3Sb_5, within the same birefrigence domain as shown in Extended Fig.6, we observe large-area two CD domains with opposite signs, which is another strong evidence of TRS breaking. Therefore, we conclude that the onset of CD at the T_{CDW} comes from TRS breaking.

Discussion

Our observation of two-fold symmetry and three-state nematicity just below T_{CDW} is very different from the nematic order observed by STM in CsV_3Sb_5[53, 56] and KV_3Sb_5 [20], which shows the nematic order at temperature much below T_{CDW}. The difference is probably not just because that STM is an surface sensitive measurement, and our probe is a bulk measurement as the penetration depth of the light is around 50 nm [60, 61]. It could be that the nematicity observed by STM is some kind of additional electronically-driven phenomena at low temperature as proposed recently[20, 53, 56]. Also, the three domains were not resolved by STM[20, 53, 56]. The origin of the two-fold symmetry and three domains observed in our measurement is most likely due to the π phase shift of the stacking between CDW layers, as shown in Fig. 1b and Extended Fig.1a, because the onset temperature of birefrigence coincides with T_{CDW} in all three compounds. There have been lots of works of proposing different kinds of stacking between CDW layers [26, 30, 31, 35, 56, 57, 62–65]. Our results shows that those without two-fold symmetry are not compatible. The domains we observe are on the order of 100 μm scale, which explains the nematicity observed in transport experiments on macroscopic samples possibly due to unequal population of three domains [54, 55]. Our results add strong constrains on interpreting other macroscopic measurements including photo-emission, x-ray and optical spectroscopy [17, 26, 30, 35, 36, 57, 60, 61, 63–67].

As predicted in theoretical works [28, 45, 47, 68, 69], the interactions between saddle points in the kagome lattice lead to various competing orders such as real and chiral flux CDW orders in AV_3Sb_5. In some parameter regimes, the favored chiral flux CDW order can also induce real CDW order, leading to a mixture of order parameters. The results from our optical measurements shows that both the three-state nematicity and TRS breaking exhibit at T_{CDW} in AV_3Sb_5, which indicate that the two kinds of symmetry breaking might be interwined. The TRS breaking is favorable to the chiral flux CDW order with loop currents, which might indicate unconventional superconductivity in these compounds as the superconducting phase develops from the CDW phase. Looking forward, we hope our work will stimulate future works to study the nematicity and TRS breaking in both the CDW and superconducting phases in AV_3Sb_5. The imaging methodologies developed here can also be widely applied to other strongly correlated and topological systems.

[1] Yan, S., Huse, D. A. & White, S. R. Spin-liquid ground state of the S = 1/2 kagome heisenberg antiferromagnet. *Science* **332**, 1173–1176 (2011).

[2] Han, T. H. *et al.* Fractionalized excitations in the spin-liquid state of a kagome-lattice antiferromagnet. *Nature 2012 492:7429* **492**, 406–410 (2012). 1307.5047.

[3] Shores, M. P., Nytko, E. A., Bartlett, B. M. & Nocera, D. G. A structurally perfect S = 1/2 Kagomé antiferromagnet. *Journal of the American Chemical Society* **127**, 13462–13463 (2005).

[4] Yin, J. X. *et al.* Giant and anisotropic many-body spin–orbit tunability in a strongly correlated kagome magnet. *Nature 2018 562:7725* **562**, 91–95 (2018).

[5] Yin, J. X. *et al.* Negative flat band magnetism in a spin–orbit-coupled correlated kagome magnet. *Nature Physics 2019 15:5* **15**, 443–448 (2019).

[6] Yin, J. X. *et al.* Quantum-limit Chern topological magnetism in TbMn$_6$Sn$_6$. *Nature 2020 583:7817* **583**, 533–536 (2020).

[7] Yin, J. X. *et al.* Quantum-limit Chern topological magnetism in TbMn$_6$Sn$_6$. *Nature 2020 583:7817* **583**, 533–536 (2020).

[8] Yin, J. X., Pan, S. H. & Zahid Hasan, M. Probing topological quantum matter with scanning tunnelling microscopy. *Nature Reviews Physics 2021 3:4* **3**, 249–263 (2021). 2103.08646.

[9] Ye, L. *et al.* Massive Dirac fermions in a ferromagnetic kagome metal. *Nature 2018 555:7698* **555**, 638–642 (2018). 1709.10007.

[10] Ghimire, N. J. & Mazin, I. I. Topology and correlations on the kagome lattice. *Nature Materials 2020 19:2* **19**, 137–138 (2020).

[11] Nakatsuji, S., Kiyohara, N. & Higo, T. Large anomalous Hall effect in a non-collinear antiferromagnet at room temperature. *Nature 2015 527:7577* **527**, 212–215 (2015).

[12] Mielke, C. *et al.* Nodeless kagome superconductivity in LaRu$_3$Si$_2$. *Physical Review Materials* **5**, 034803 (2021).

[13] Guguchia, Z. *et al.* Tunable anomalous Hall conductivity through volume-wise magnetic competition in a topological kagome magnet. *Nature Communications 2020 11:1* **11**, 1–9 (2020).

[14] Ortiz, B. R. *et al.* CsV$_3$Sb$_5$: A $\mathbb{Z}_2$ Topological Kagome Metal with a Superconducting Ground State. *Physical Review Letters* **125**, 247002 (2020).

[15] Ortiz, B. R. *et al.* Superconductivity in the $\mathbb{Z}_2$ kagome metal KV$_3$Sb$_5$. *Phys. Rev. Materials* **5**, 034801 (2021).

[16] Hu, Y. *et al.* Rich nature of van hove singularities in kagome superconductor CsV$_3$Sb$_5$ (2021). 2106.05922.

[17] Kang, M. *et al.* Twofold van hove singularity and origin of charge order in topological kagome superconductor CsV$_3$Sb$_5$. *Nature Physics* (2022).

[18] Hao, Z. *et al.* Dirac nodal lines and nodal loops in a topological kagome superconductor CsV$_3$Sb$_5$ (2021). 2111.02639.

[19] Jiang, Y. X. *et al.* Unconventional chiral charge order in kagome superconductor KV$_3$Sb$_5$. *Nature Materials 2021 20:10* **20**, 1353–1357 (2021).

[20] Li, H. *et al.* Rotation symmetry breaking in the normal state of a kagome superconductor KV$_3$Sb$_5$. *Nature Physics* (2022).

[21] Xu, H.-S. *et al.* Multiband superconductivity with sign-preserving order parameter in kagome superconductor CsV$_3$Sb$_5$. *Phys. Rev. Lett.* **127**, 187004 (2021).

[22] Liu, Z. *et al.* Charge-density-wave-induced bands renormalization and energy gaps in a kagome superconductor RbV$_3$Sb$_5$. *Phys. Rev. X* **11**, 041010 (2021).

[23] Shumiya, N. *et al.* Intrinsic nature of chiral charge order in the kagome superconductor RbV$_3$Sb$_5$. *Phys. Rev. B* **104**, 035131 (2021).

[24] Wang, Z. *et al.* Electronic nature of chiral charge order in the kagome superconductor CsV$_3$Sb$_5$. *Phys. Rev. B* **104**, 075148 (2021).

[25] Wang, Q. *et al.* Charge density wave orders and enhanced superconductivity under pressure in the kagome metal CsV$_3$Sb$_5$. *Advanced Materials* **33**, 2102813 (2021).

[26] Liang, Z. *et al.* Three-Dimensional Charge Density Wave and Surface-Dependent Vortex-Core States in a Kagome Superconductor CsV$_3$Sb$_5$. *Physical Review X* **11**, 031026 (2021).

[27] Tan, H., Liu, Y., Wang, Z. & Yan, B. Charge Density Waves and Electronic Properties of Superconducting Kagome Metals. *Physical Review Letters* **127**, 046401 (2021). 2103.06325.

[28] Lin, Y.-P. & Nandkishore, R. M. Complex charge density waves at van hove singularity on hexagonal lattices: Haldane-model phase diagram and potential realization in the kagome metals AV$_3$Sb$_5$ (A=K, Rb, Cs). *Phys. Rev. B* **104**, 045122 (2021).

[29] Wang, Z. *et al.* Distinctive momentum dependent charge-density-wave gap observed in CsV$_3$Sb$_5$ superconductor with topological kagome lattice (2021). 2104.05556.

[30] Ortiz, B. R. *et al.* Fermi surface mapping and the nature of charge-density-wave order in the kagome superconductor CsV$_3$Sb$_5$. *Phys. Rev. X* **11**, 041030 (2021).

[31] Luo, J. *et al.* Star-of-david pattern charge density wave with additional modulation in the kagome superconductor CsV$_3$Sb$_5$ revealed by ^{51}V-nmr and $^{121/123}$Sb-nqr (2021). 2108.10263.

[32] Nakayama, K. *et al.* Multiple energy scales and anisotropic energy gap in the charge-density-wave phase of the kagome superconductor CsV$_3$Sb$_5$. *Phys. Rev. B* **104**, L161112 (2021).

[33] Luo, Y. *et al.* Distinct band reconstructions in kagome superconductor CsV$_3$Sb$_5$ (2021). 2106.01248.

[34] Lou, R. *et al.* Charge-density-wave-induced peak-dip-hump structure and the multiband superconductivity in a kagome superconductor CsV$_3$Sb$_5$. *Phys. Rev. Lett.* **128**, 036402 (2022).

[35] Miao, H. *et al.* Geometry of the charge density wave in the kagome metal AV$_3$Sb$_5$. *Phys. Rev. B* **104**, 195132 (2021).

[36] Luo, H. *et al.* Electronic nature of charge density wave and electron-phonon coupling in kagome superconductor KV$_3$Sb$_5$. *Nature Communications* **13**, 273 (2022).

[37] Yu, J. *et al.* Evolution of electronic structure in pristine and hole-doped kagome metal RbV$_3$Sb$_5$ (2021). 2109.11286.

[38] Ortiz, B. R. *et al.* New kagome prototype materials: Discovery of KV$_3$Sb$_5$,RbV$_3$Sb$_5$, and CsV$_3$Sb$_5$. *Physical Review Materials* **3**, 094407 (2019).

[39] Zhao, C. C. *et al.* Nodal superconductivity and superconducting domes in the topological kagome metal CsV$_3$Sb$_5$ (2021). 2102.08356.

[40] Chen, H. *et al.* Roton pair density wave in a strong-coupling kagome superconductor. *Nature* **599**, 222–228 (2021).

[41] Yin, Q. *et al.* Superconductivity and normal-state properties of kagome metal RbV$_3$Sb$_5$ single crystals. *Chinese Physics Letters* **38**, 037403 (2021).

[42] Belopolski, I. *et al.* Discovery of topological weyl fermion lines and drumhead surface states in a room temperature magnet. *Science* **365**, 1278–1281 (2019).

[43] Morali, N. *et al.* Fermi-arc diversity on surface terminations of the magnetic weyl semimetal Co$_3$Sn$_2$S$_2$. *arXiv preprint arXiv:1903.00509* (2019).

[44] Varma, C. Non-Fermi-liquid states and pairing instability of a general model of copper oxide metals. *Physical Review B* **55**, 14554 (1997).

[45] Park, T., Ye, M. & Balents, L. Electronic instabilities of kagome metals: Saddle points and landau theory. *Phys. Rev. B* **104**, 035142 (2021).

[46] Feng, X., Jiang, K., Wang, Z. & Hu, J. Chiral flux phase in the kagome superconductor AV$_3$Sb$_5$. *Science Bulletin* **66**, 1384–1388 (2021).

[47] Denner, M. M., Thomale, R. & Neupert, T. Analysis of charge order in the kagome metal AV$_3$Sb$_5$ (A = K, Rb, Cs). *Phys. Rev. Lett.* **127**, 217601 (2021).

[48] Mielke, C. *et al.* Time-reversal symmetry-breaking charge order in a kagome superconductor. *Nature* **602**, 245–250 (2022).

[49] Yu, L. *et al.* Evidence of a hidden flux phase in the topological kagome metal CsV$_3$Sb$_5$ (2021). 2107.10714.

[50] Yang, S.-Y. *et al.* Giant, unconventional anomalous hall effect in the metallic frustrated magnet candidate, KV$_3$Sb$_5$. *Science advances* **6**, eabb6003 (2020).

[51] Yu, F. H. *et al.* Concurrence of anomalous hall effect and charge density wave in a superconducting topological kagome metal. *Phys. Rev. B* **104**, L041103 (2021).

[52] Wu, Q. *et al.* The large static and pump-probe kerr effect with two-fold rotation symmetry in kagome metal CsV$_3$Sb$_5$ (2021). 2110.11306.

[53] Zhao, H. *et al.* Cascade of correlated electron states in the kagome superconductor CsV$_3$Sb$_5$. *Nature 2021 599:7884*

599, 216–221 (2021). 2103.03118.

[54] Xiang, Y. *et al.* Twofold symmetry of c-axis resistivity in topological kagome superconductor CsV_3Sb_5 with in-plane rotating magnetic field. *Nature Communications 2021 12:1* **12**, 1–8 (2021). 2104.06909.

[55] Ni, S. *et al.* Anisotropic superconducting properties of kagome metal CsV_3Sb_5. *Chinese Physics Letters* **38**, 057403 (2021).

[56] Nie, L. *et al.* Charge-density-wave-driven electronic nematicity in a kagome superconductor. *Nature* (2022).

[57] Kang, M. *et al.* Microscopic structure of three-dimensional charge order in kagome superconductor AV_3Sb_5 and its tunability (2022). 2202.01902.

[58] Ni, Z. *et al.* Direct imaging of antiferromagnetic domains and anomalous layer-dependent mirror symmetry breaking in atomically thin $MnPS_3$. *Phys. Rev. Lett.* **127**, 187201 (2021).

[59] Ni, Z. *et al.* Imaging the néel vector switching in the monolayer antiferromagnet $MnPSe_3$ with strain-controlled ising order. *Nature Nanotechnology* **16**, 782–787 (2021).

[60] Zhou, X. *et al.* Origin of charge density wave in the kagome metal CsV_3Sb_5 as revealed by optical spectroscopy. *Phys. Rev. B* **104**, L041101 (2021).

[61] Uykur, E., Ortiz, B. R., Wilson, S. D., Dressel, M. & Tsirlin, A. A. Optical detection of the density-wave instability in the kagome metal KV_3Sb_5. *npj Quantum Materials* **7**, 16 (2022).

[62] Ratcliff, N., Hallett, L., Ortiz, B. R., Wilson, S. D. & Harter, J. W. Coherent phonon spectroscopy and interlayer modulation of charge density wave order in the kagome metal CsV_3Sb_5. *Phys. Rev. Materials* **5**, L111801 (2021).

[63] Li, H. *et al.* Spatial symmetry constraint of charge-ordered kagome superconductor CsV_3Sb_5. *arXiv e-prints* arXiv:2109.03418 (2021). 2109.03418.

[64] Li, H. *et al.* Observation of Unconventional Charge Density Wave without Acoustic Phonon Anomaly in Kagome Superconductors AV_3Sb_5 (A=Rb, Cs). *Physical Review X* **11**, 031050 (2021). 2103.09769.

[65] Xiao, Q. *et al.* Coexistence of Multiple Stacking Charge Density Waves in Kagome Superconductor CsV_3Sb_5. *arXiv e-prints* arXiv:2201.05211 (2022). 2201.05211.

[66] Nakayama, K. *et al.* Carrier injection and manipulation of charge-density wave in kagome superconductor CsV_3Sb_5. *Phys. Rev. X* **12**, 011001 (2022).

[67] Wu, S. *et al.* Charge density wave order in kagome metal AV_3Sb_5 (A= Cs, Rb, K) (2022). 2201.05188.

[68] Setty, C., Hu, H., Chen, L. & Si, Q. Electron correlations and T-breaking density wave order in a $\mathbb{Z}_2$ kagome metal (2021). 2105.15204.

[69] Kiesel, M. L., Platt, C. & Thomale, R. Unconventional fermi surface instabilities in the kagome hubbard model. *Phys. Rev. Lett.* **110**, 126405 (2013).

[70] Jin, C. *et al.* Stripe phases in WSe_2/WS_2 moiré superlattices. *Nature Materials 2021 20:7* **20**, 940–944 (2021). 2007.12068.
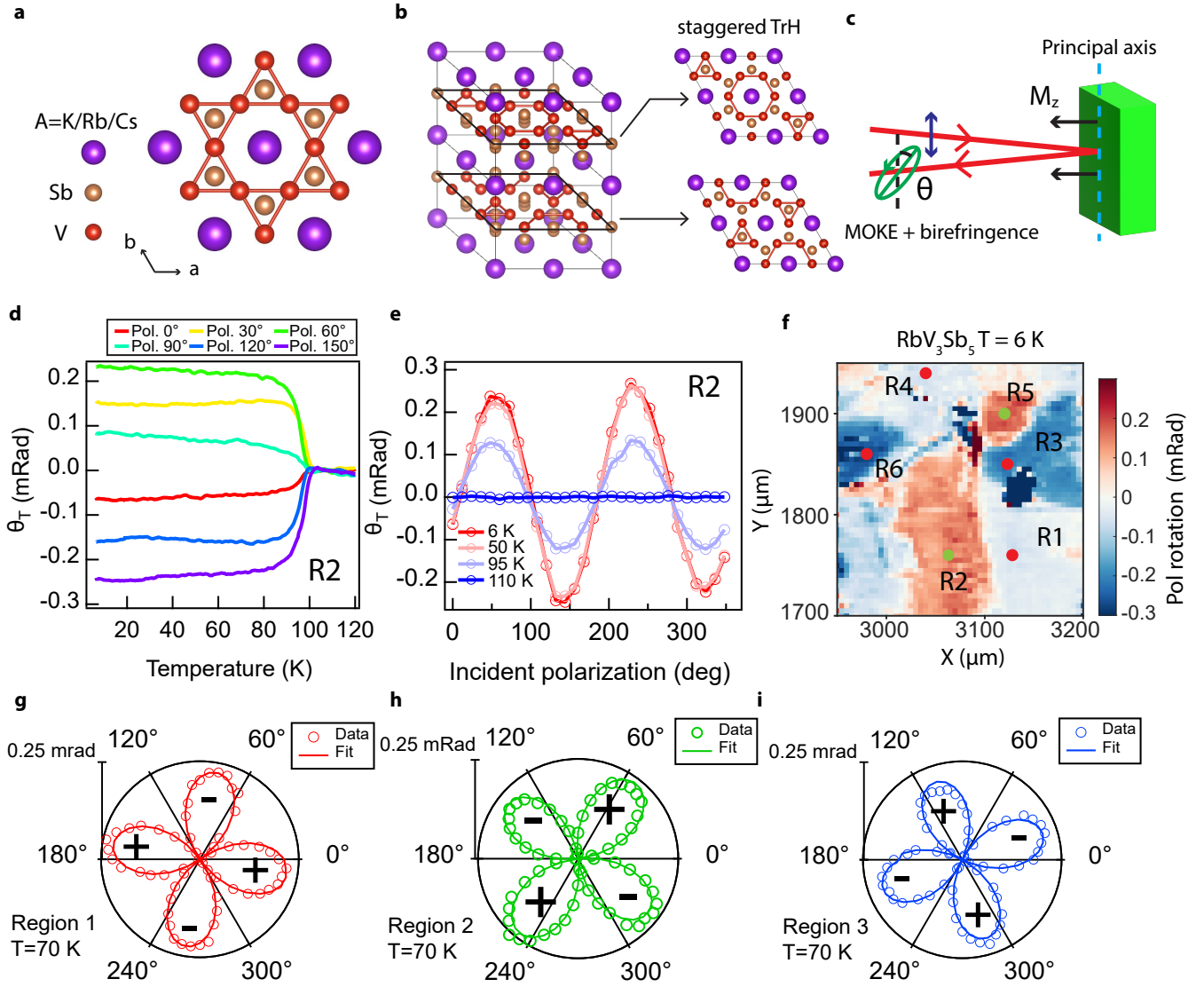
FIG. 1: **Three-state nematic order in RbV$_3$Sb$_5$.** (a) Top view of the kagome lattice structure (a-b plane) of AV$_3$Sb$_5$ (A=K, Rb, Cs). The V$_3$Sb and K/Rb/Cs layers form the kagome and triangular lattices, respectively. (b) A 3D crystal structure showing an staggered tri-hexagonal (TrH) CDW order. There is a relative phase of π shift between the neighboring in-plane 2×2 TrH CDW orders. (c) A schematic shows the change of polarization angle θ_T due to a combination of magneto-optical Kerr effect and the birefringence effect. (d) θ_T vs temperature measured at the green spot in region 2 in (f) with different incident polarization. (e) θ_T vs incident polarization at different temperature. The plot is obtained from averaging the data shown in (d) in a ±1 K window centered around the labeled temperature. (f) Spatial mapping of θ_T at T= 6 K in a RbV$_3$Sb$_5$ sample measured at an incident polarization of ϕ=37.6°, which corresponds to zero birefrigence in R1. Six regions are labeled as R1 to R6, and the red/green spots indicate the positions where the birefringence measurement within each domain are performed. The two dark blue islands are caused by impurities on the surface (see optical images in Extended Fig. 1). (g-i) Polar plots of the birefringence patterns at T= 70 K at the marked red/green dots in regions 1-3, respectively. The + and - symbols show the sign of θ_T.
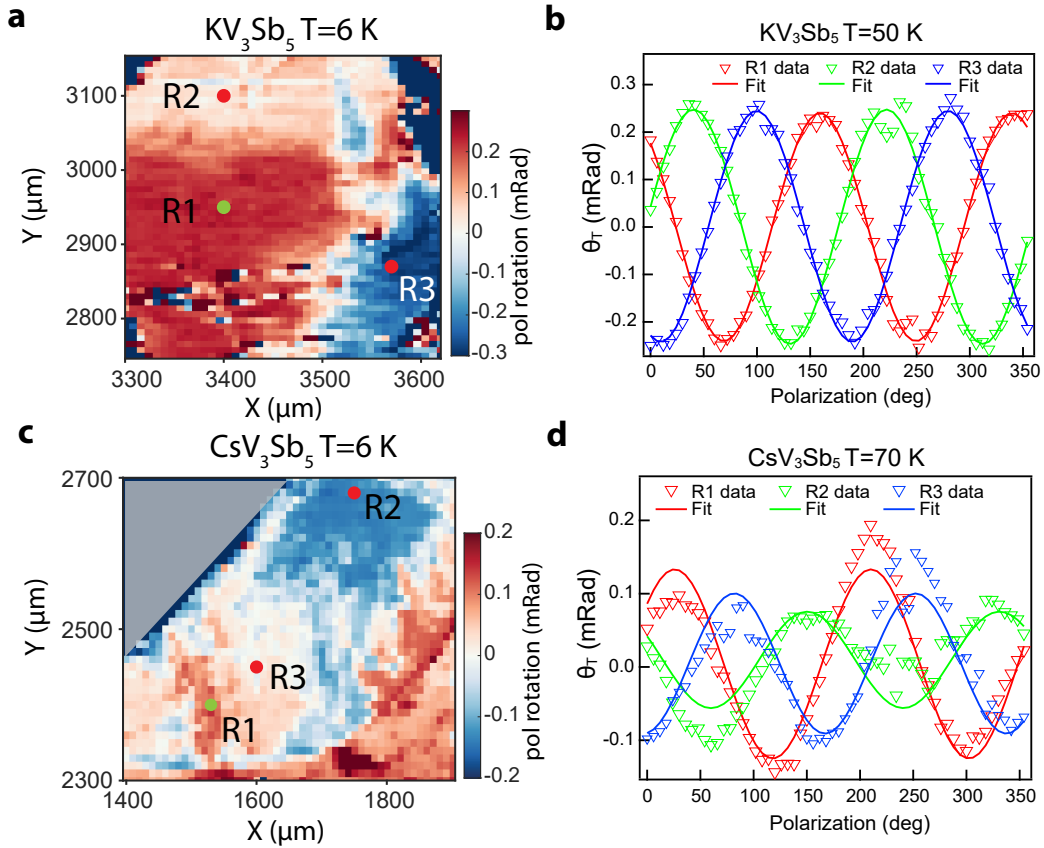
FIG. 2: **Three-state nematic order in KV$_3$Sb$_5$ and CsV$_3$Sb$_5$.** (a, c) Spatial mapping of θ_T at T= 6 K in KV$_3$Sb$_5$ and CsV$_3$Sb$_5$ measured at incident polarizations of 0° and 46°, respectively. Three domains are labelled as R1, R2 and R3. The red/green spots indicate the positions where the birefringence measurements (see panels b and d) are performed. The gray triangle in panel (c) indicates region off the sample. (b, d) Birefringence patterns of KV$_3$Sb$_5$ and CsV$_3$Sb$_5$ measured at T= 50 K and T= 70 K at green/red dots in regions 1-3, respectively.
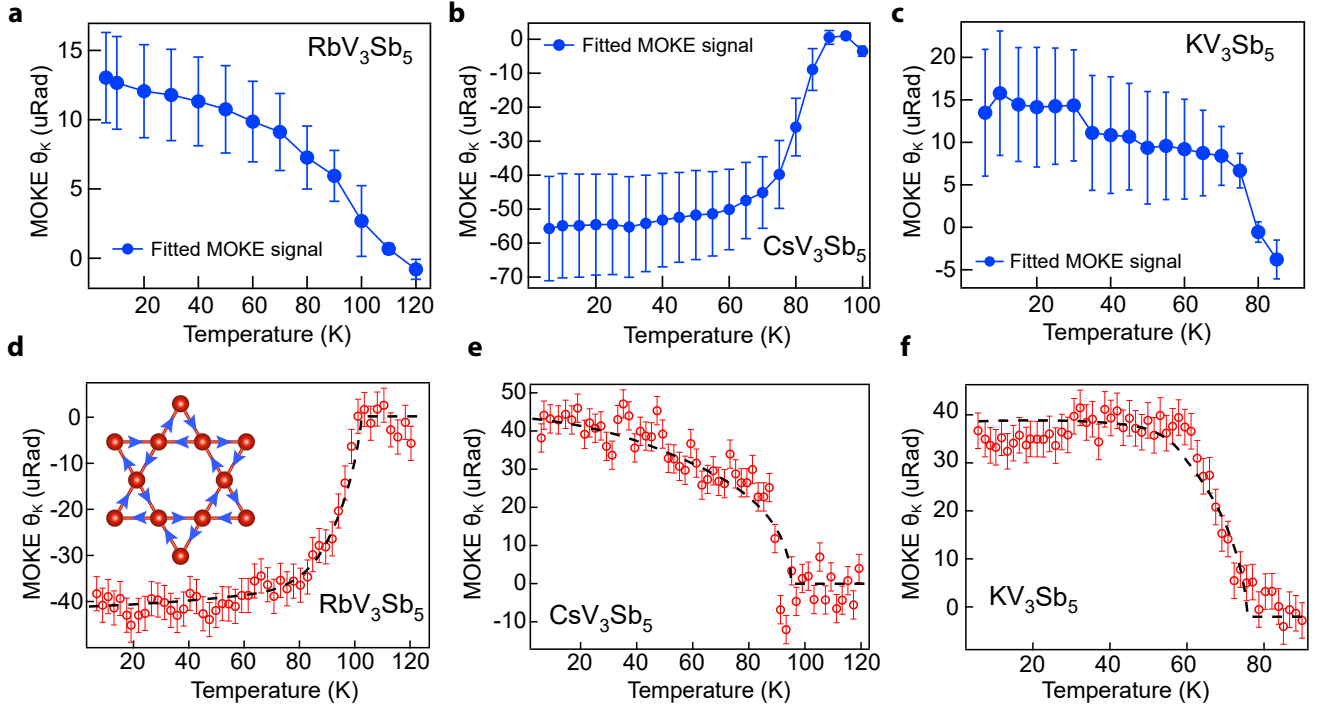
FIG. 3: **MOKE in AV$_3$Sb$_5$.** (a-c) Fitted MOKE signal θ_K vs temperature with error bars for K, Rb and Cs compounds, respectively. The error bar is defined as the fitting error of θ_K by Eq. 1. (d-f) MOKE signal vs temperature measured at the incident angles with zero birefringence for K, Rb and Cs compounds, respectively. The inset in panel d shows the orbital currents (blue arrows) in the kagome lattice. The error bar is 3.7 uRad as defined in the main text, which is larger than the standard deviation of the θ_K from 6-40 K
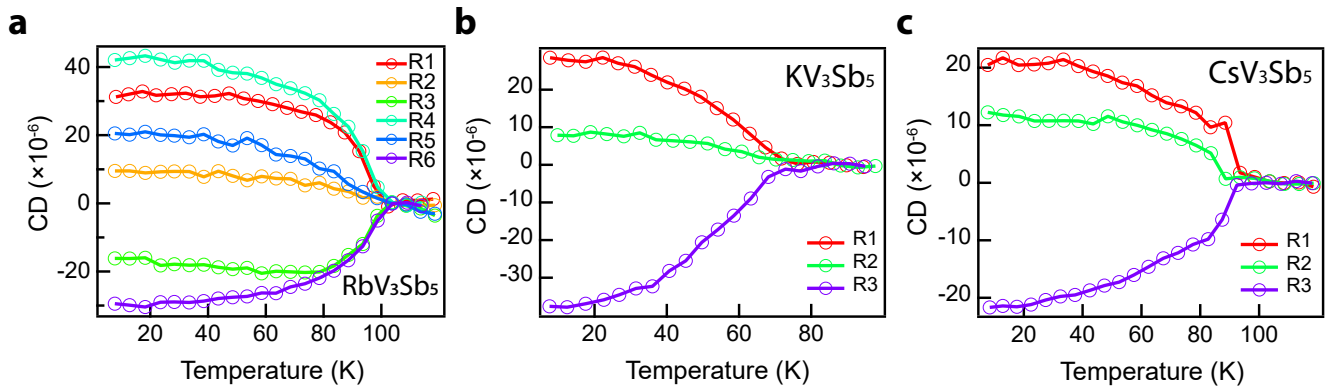
FIG. 4: **Circular dichroism in AV$_3$Sb$_5$.** (a) Circular dichroism vs temperature measured at the corresponding spots in region 1-6 in Extended Fig. 5(a) in RbV$_3$Sb$_5$. (b-c) Circular dichroism vs temperature at the selected spots in region 1-3 in KV$_3$Sb$_5$ and CsV$_3$Sb$_5$ in Extended Fig. 5(b) and (c), respectively. The error bar is smaller than the symbol size of the data point in a-c.
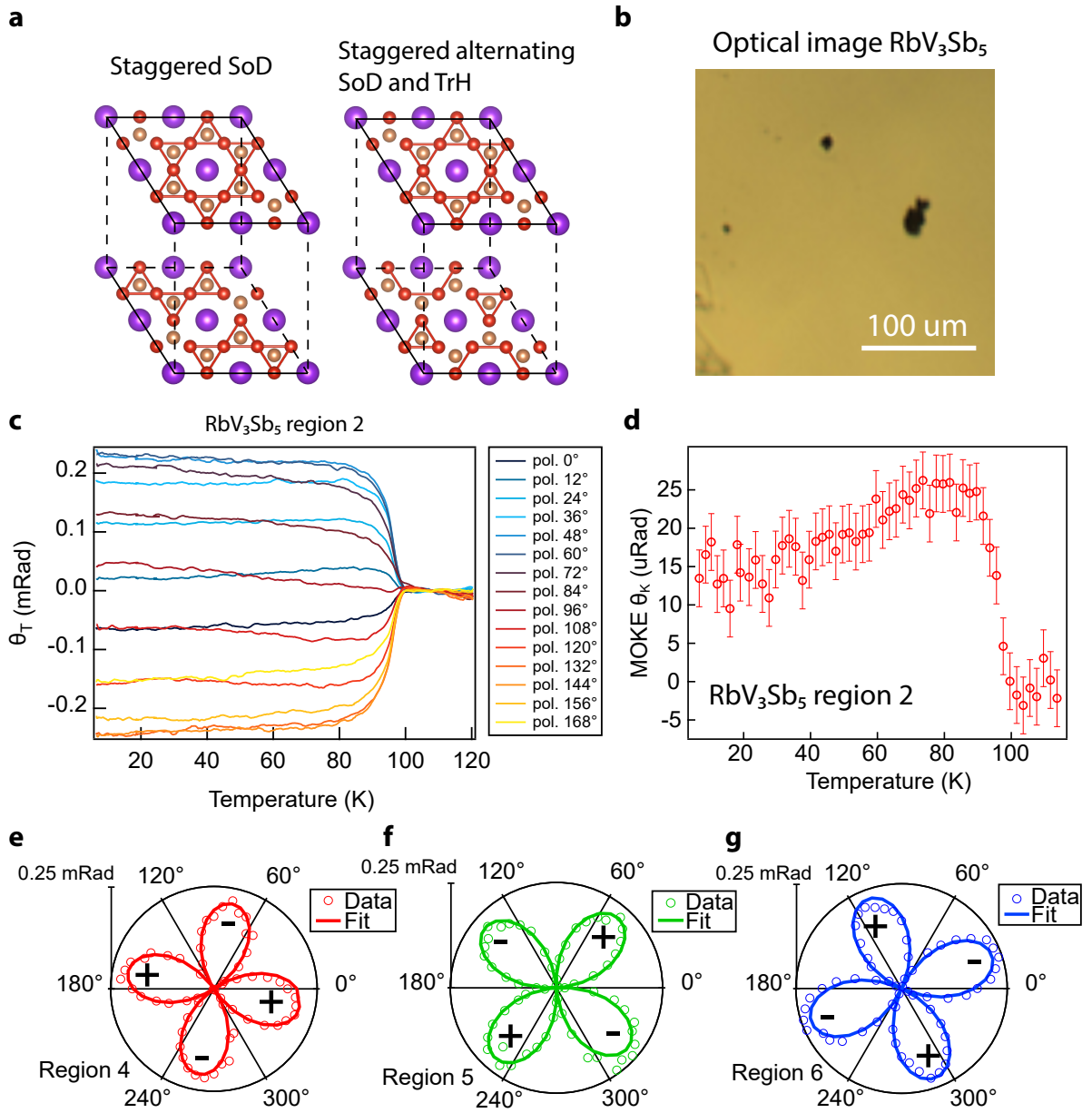
Extended Data Figure 1: (a) 3D lattice structures showing two other possible staggered CDW orders with a π phase shift, the staggered SoD and the staggered alternating SoD and TrH CDW orders. (b) Optical image of the mapping region in Fig. 1 (f) in RbV_3Sb_5. The black dots indicate impurities on the surface. (c) θ_T vs temperature for various incident polarization measured in region 2 in RbV_3Sb_5. (d) MOKE signal vs temperature measured at the zero birefringence incident angle in region 2 in RbV_3Sb_5. The error bar is 3.7 uRad (see main text for definition of error). (e-g) Polar plots of the birefringence patterns at T=70 K measured at the corresponding spots in region 4, 5 and 6 (see Fig. 1(f)), respectively.
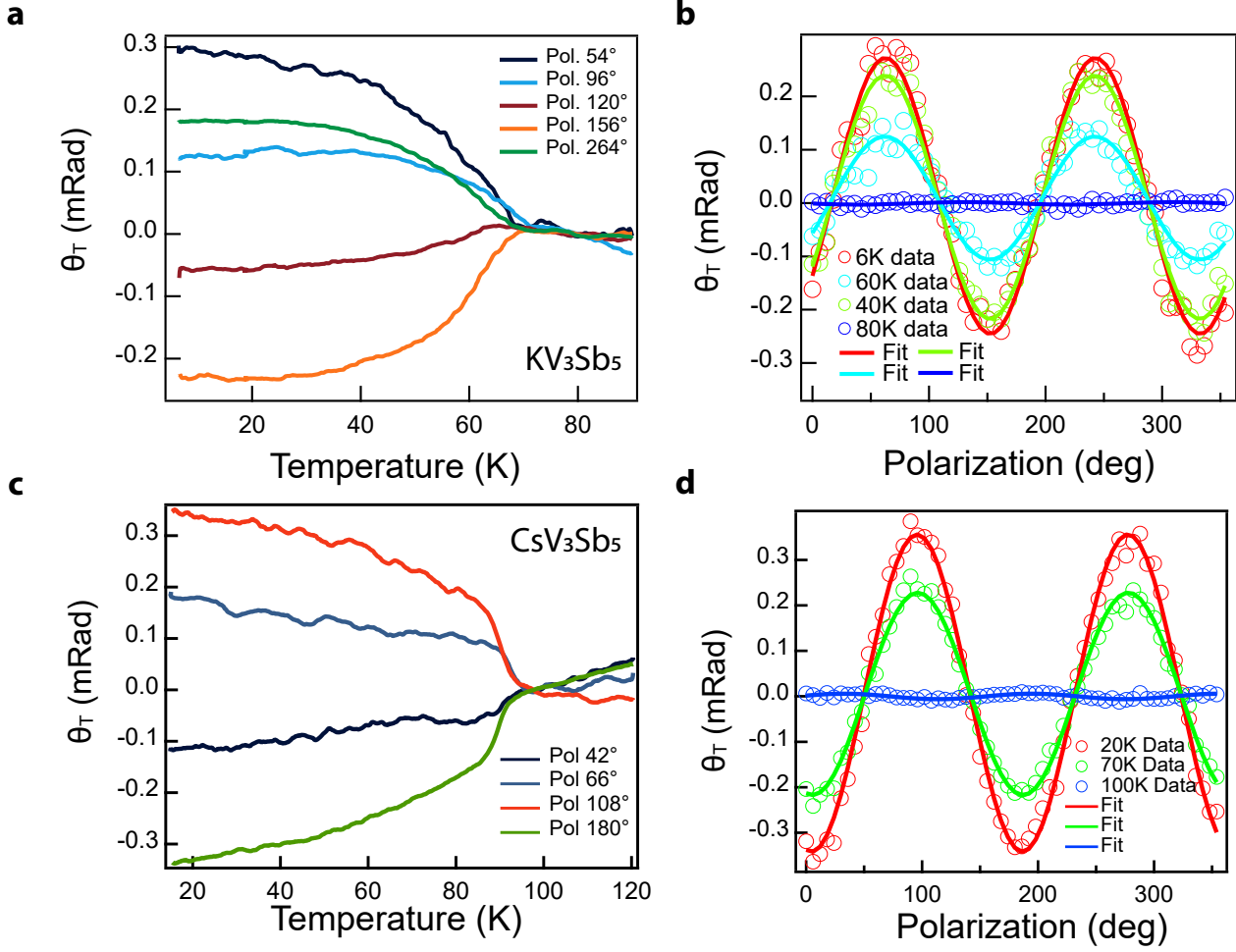
Extended Data Figure 2: (a, c) θ_T vs temperature for various incident polarization for KV_3Sb_5 and CsV_3Sb_5, respectively. (b, d) θ_T vs incident polarization at different temperature cuts for KV_3Sb_5 and CsV_3Sb_5, respectively.
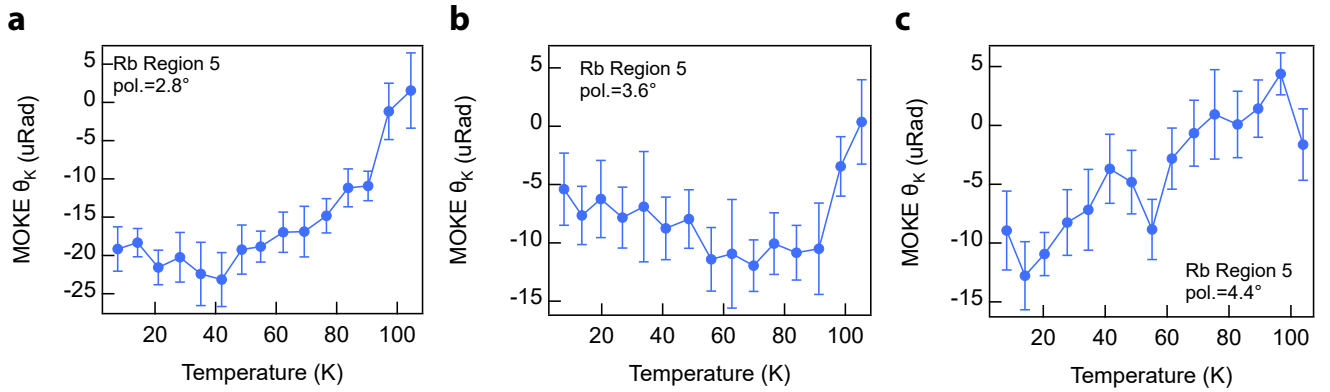

Extended Data Figure 3: (a-c) MOKE signal measured at the incident angles $\phi_0 = 3.6°$ and $\phi_0 \pm 0.8$ in region 5 for RbV_3Sb_5, where ϕ_0 is the incident angle that birefringence contribution is zero. The error bar is defined as the statistical error for data points averaged together over 2 K range bins.
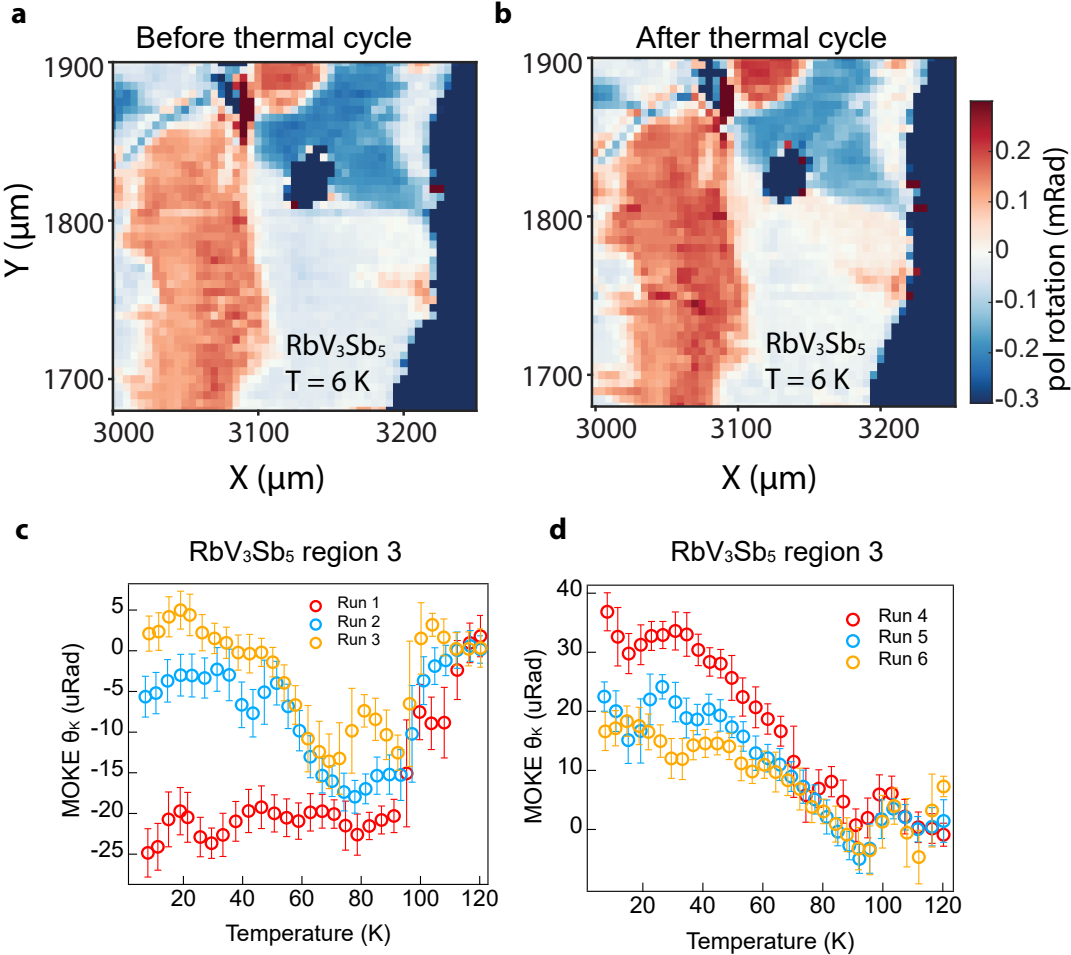
Extended Data Figure 4: (a-b) Spatial mapping of θ_T at T = 6 K, before and after thermal cycles for RbV$_3$Sb$_5$. (c-d) MOKE signal vs temperature for run 1-3 and run 4-6 measured at one selected location in region 3, respectively. The incident angle for zero birefringence is at 242.8°. The error bar is defined as the statistical error for data points averaged together over 8 K range bins. The non-monotonic trend in run 2 and 3 are probably because the laser spot hits two time-reversed domains.
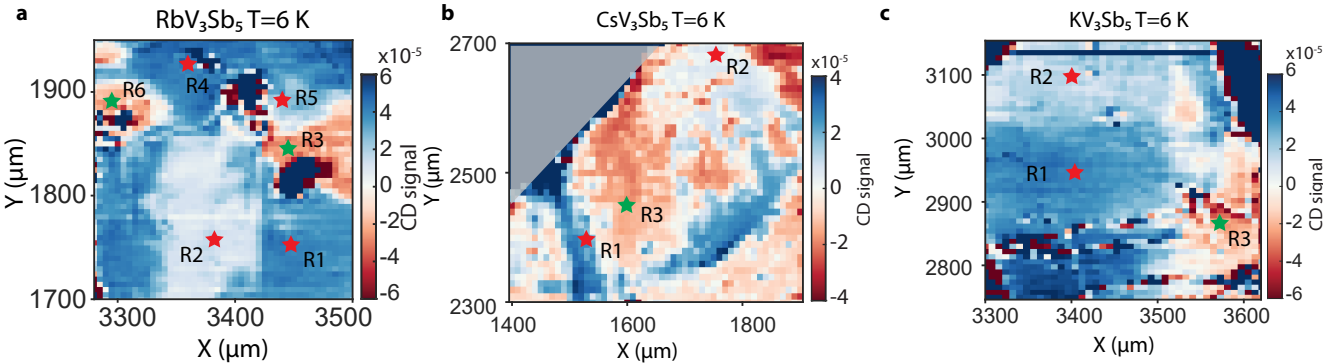
Extended Data Figure 5: (a-c) Circular dichroism maps at T= 6 K for Rb, K and Cs compounds, respectively. The red and green star symbols indicate the positions where circular dichroism vs temperature measurements are performed in Fig. 4.

a

Birefringence map

b

CD map

c

d
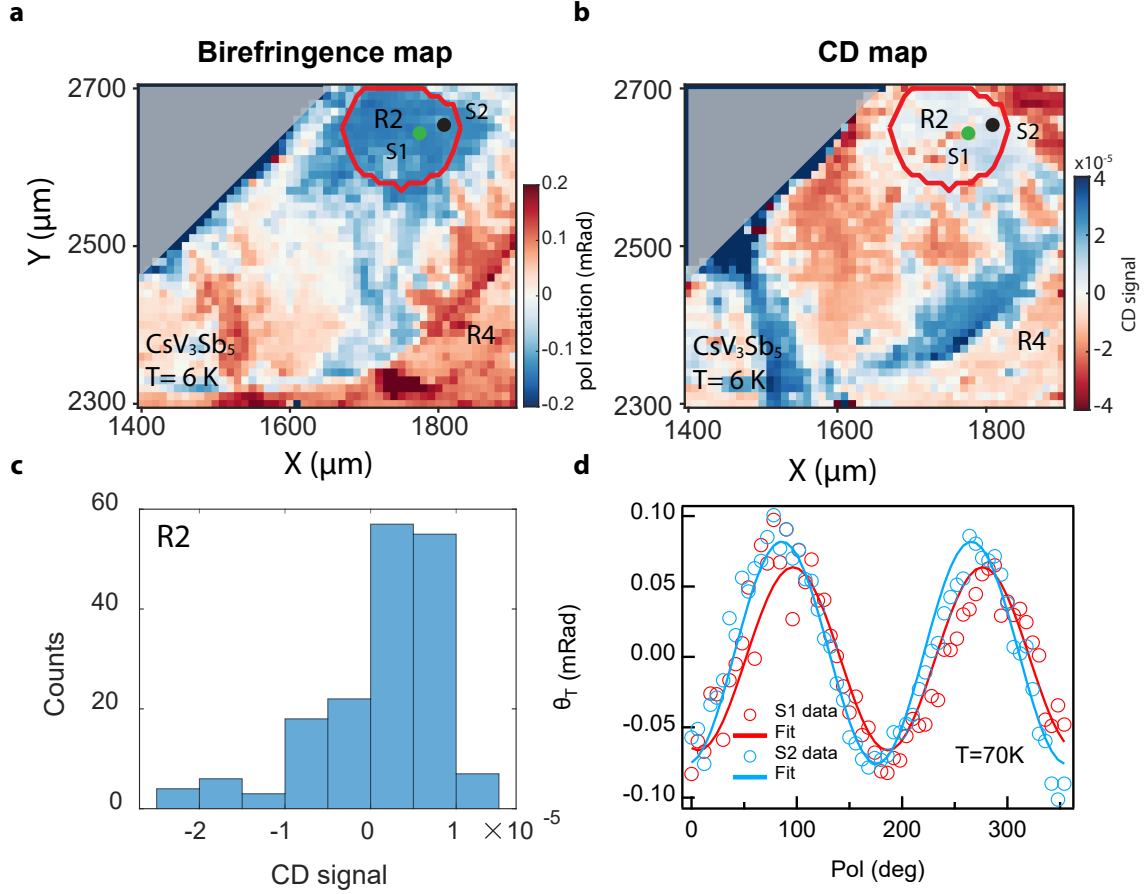
Extended Data Figure 6: (a-b) The spatial birefringence and circular dichroism maps of CsV_3Sb_5 at T = 6 K, respectively. The region circled by red is region 2, where points within each region have the same birefringence pattern. The green and black dots indicate two spots in R2 (S1 and S2), which have same birefringence patterns but opposite signs of CD signal. (c) Histograms of circular dichroism signals within region 2. Both positive and negative CD signals within R2. (d) θ_T vs incident polarization at T= 70 K measured at S1 and S2 within R2, respectively.

a

b

c
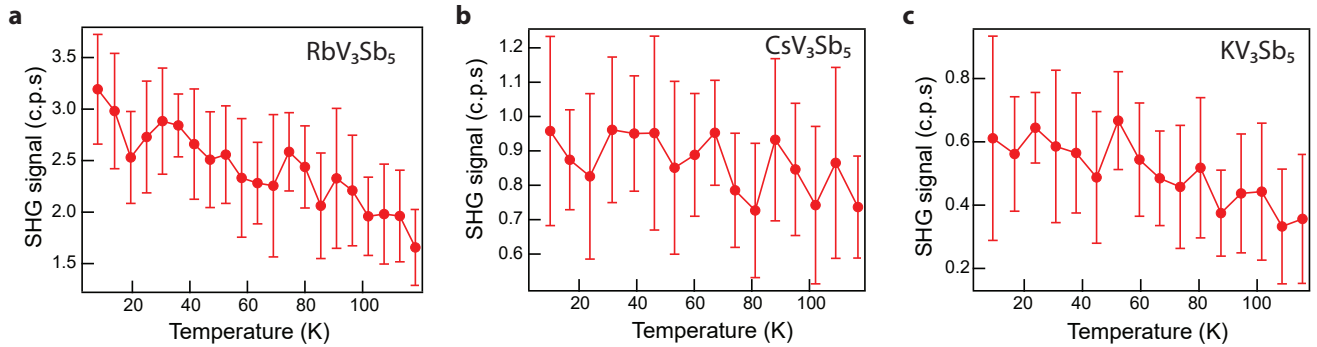
Extended Data Figure 7: Second harmonic generation of AV_3Sb_5. (a-c) Second harmonic generation vs temperature for Rb, Cs and K compounds, respectively. The error bar is defined as the statistical error for data points averaged together over 5 K range bins.

I. METHODS

A. Sample growth method

Single crystals of CsV_3Sb_5, RbV_3Sb_5, and KV_3Sb_5 were synthesized from Cs (liquid, Alfa 99.98%), Rb (liquid, Alfa 99.75%), K (metal, Alfa 99.95%), V (powder, Sigma 99.9%) and Sb (shot, Alfa 99.999%). As-received vanadium powder was purified in-house to remove residual oxides. Due to extreme reactivity of elemental alkalis, all further preparation of AV_3Sb_5 crystals were performed in an argon glovebox with oxygen and moisture levels <0.5 ppm. AV_3Sb_5 single crystals were synthesized using the self-flux method. Elemental reagents were milled in a pre-seasoned tungsten carbide vial to form a composition which is 50 at.% $A_{0.4}Sb_{0.6}$ and approximately 50 at.% VSb_2. Excess antimony can be added to the flux to suppress volatility if needed. The fluxes were loaded into alumina crucibles and sealed within stainless steel jackets. The samples were heated to 1000 ° C at 250 ° C/hr and soaked there for 24 h. The samples were subsequently cooled to 900 ° C at 100 ° C/hr and then further to 500 ° C at 1 ° C/hr. Once cooled, the crystals are recovered mechanically. Crystals are hexagonal flakes with brilliant metallic luster. Elemental composition of the crystals was assessed using energy dispersive x-ray spectroscopy (EDX) using a APREOC scanning electron microscope.

B. Birefringence and MOKE measurements

Laser pulses from a Ti:sapphire oscillator with 800 nm center wavelength, 80 MHz repetition rate and 50 fs pulse duration are used to measure the change of polarization angle. To measure the change of the polarization angle without rotating the sample, a half wave plate (HWP) is put right in front of the sample and in between the cube beam splitter. Both the incident and reflected light goes through the half wave plate, thus polarization change due to the half wave plate is cancelled. The net change of the polarization purely comes from the sample itself [70]. By rotating the HWP, we can measure the change of polarization θ_T for different incident polarizations.

In the following derivation, we will show how the birefringence and the MOKE signal can be distinguished by rotating the half wave plate and keeping the beam at the same spot. The Jones matrix for polarizer at 45° and 0°, photo-elastic modulator (PEM), half wave plate (α) and mirror are,

$$P(45) = \frac{1}{2}\begin{bmatrix} 1 & 1 \\ 1 & 1 \end{bmatrix}$$

$$P(0) = \begin{bmatrix} 1 & 0 \\ 0 & 0 \end{bmatrix}$$

$$HWP(\alpha) = \begin{bmatrix} \cos(2\alpha) & \sin(2\alpha) \\ \sin(2\alpha) & -\cos(2\alpha) \end{bmatrix}$$

$$PEM = \begin{bmatrix} 1 & 0 \\ 0 & e^{i\tau} \end{bmatrix}$$

$$M = \begin{bmatrix} 1 & 0 \\ 0 & -1 \end{bmatrix}$$

where α is the angle between the fast axis of the half wave plate and the horizontal axis of the lab, τ is the phase retardation applied by the PEM. The rotation matrix is,

$$R(\beta) = \begin{bmatrix} \cos(\beta) & -\sin(\beta) \\ \sin(\beta) & \cos(\beta) \end{bmatrix}$$

where β is the angle of rotation. For a sample that has both the birefringence and MOKE effect, we can use the following Jones matrix to represent the sample (ignoring the higher order term),

$$S(\theta) = \begin{bmatrix} 1 - \sin(\theta)^2\Delta & \frac{\Delta\sin(2\theta)}{2} - c \\ \frac{\Delta\sin(2\theta)}{2} + c & 1 - \cos(\theta)^2\Delta \end{bmatrix} \quad (2)$$

where θ is the angle between the fast axis and the polarization of the incident light, $\Delta = \delta + i\kappa$ is the complex birefringence term, and $c = \theta_K + i\eta$ comes from the MOKE effect which is also a complex number. The output light O measured at the photo detector can be calculated by,

$$O = P(0) \cdot HWP(\pi - \alpha) \cdot M \cdot S(\theta) \cdot HWP(\alpha)$$

$$\cdot PEM \cdot P(45) \cdot \begin{bmatrix} E \\ 0 \end{bmatrix}$$

$$= E \begin{bmatrix} \frac{\Delta\cos(4\alpha - 2\theta)}{4} + \frac{c\,e^{\tau\,i}}{2} - \frac{\Delta}{4} + \frac{\Delta\,e^{\tau\,i}\sin(4\alpha - 2\theta)}{4} + \frac{1}{2} \\ 0 \end{bmatrix}$$

We see that the above expression only depends on the angle difference term $4\alpha - 2\theta$, thus we can set $\theta = 0$ and it will not affect the final results. The intensity measured at the photo detector is (ignoring the higher order terms),

$$I(t) = |O|^2 = E^2 \Big[\sin(\tau)\left(-\frac{\eta}{2} - \frac{\kappa\sin(4\alpha)}{4}\right)$$

$$+ \cos(\tau)\left(\frac{\theta_K}{2} + \frac{\delta\sin(4\alpha)}{4}\right) + \frac{\delta\cos(4\alpha)}{4} - \frac{\delta}{4}$$

$$+ \frac{1}{4}\Big] + \mathcal{O}(h)$$

Setting $\tau = \tau_0\sin(\omega t)$, and using the Fourier decomposition of $\cos(\tau(t))$ and $\sin(\tau(t))$, we have the following

relation,

$$I(t) = E^2 \left[\frac{\delta \cos(4\alpha)}{4} - \frac{\delta}{4} + \frac{1}{4} \right.$$
$$+ 2J_1(\tau_0)\sin(\omega t)\left(-\frac{\eta}{2} - \frac{\kappa \sin(4\alpha)}{4} \right)$$
$$\left. + (J_0(\tau_0) + 2J_2(\tau_0)\cos(2\omega t))\left(\frac{\theta_K}{2} + \frac{\delta \sin(4\alpha)}{4} \right) \right]$$
$$+ \mathcal{O}(h)$$

The $1f, 2f$ and DC component of the signal is,

$$I(1f) = E^2 2J_1(\tau_0)\left(-\frac{\eta}{2} - \frac{\kappa \sin(4\alpha)}{4} \right)\sin(\omega t)$$
$$I(2f) = E^2 2J_2(\tau_0)\left(\frac{\theta_K}{2} + \frac{\delta \sin(4\alpha)}{4} \right)\cos(2\omega t)$$
$$I(DC) = E^2 \left[\frac{\delta \cos(4\alpha)}{4} - \frac{\delta}{4} + \frac{1}{4} \right.$$
$$\left. + J_0(\tau_0)(\frac{\theta_K}{2} + \frac{\delta \sin(4\alpha)}{4}) \right]$$

We can set $\tau_0 = 2.405$, which is the zero point for the J_0 Bessel function. Since both δ and θ_K are very small, we can approximate the DC term by $I(DC) = E^2/4$. Furthermore, lock-in measures the RMS (root-mean-square) of the signal, so we have the following relation,

$$\frac{I_{lock}(1f)}{I_{lock}(DC)} = \frac{4J_1(\tau_0)}{\sqrt{2}}\left(-\eta - \frac{\kappa \sin(4\alpha)}{2} \right) \quad (3)$$
$$\frac{I_{lock}(2f)}{I_{lock}(DC)} = \frac{4J_2(\tau_0)}{\sqrt{2}}\left(\theta_K + \frac{\delta \sin(4\alpha)}{2} \right) \quad (4)$$

Finally, we note that the polarization ϕ of the incident light changes twice as much as the change of the half wave plate angle $\phi = 2\alpha$, we have the following relation,

$$-\eta - \frac{\kappa \sin(2\phi)}{2} = \frac{\sqrt{2}}{4J_1(\tau_0)}\frac{I_{lock}(1f)}{I_{lock}(DC)} \quad (5)$$
$$\theta_K + \frac{\delta \sin(2\phi)}{2} = \frac{\sqrt{2}}{4J_2(\tau_0)}\frac{I_{lock}(2f)}{I_{lock}(DC)} \quad (6)$$

We can see that the change of the polarization angle in Eq. (6) has a constant MOKE term θ_K, and a ϕ dependent birefringence term $\delta \sin(2\phi)/2$.

C. CD measurement

An alternating left circularly polarized (LCP) and right cicurlarly polarzied (RCP) light generated by the photo elastic modular (PEM) is reflected off the sample, and the difference between the LCP and RCP intensity (CD) is measured by a photo detector connected to a lock-in analyzer. PEM modulates the incident light between the left circularly- and right circularly- polarized at a frequency of $f = 42$ kHz. Both the $1f$ and DC component is extracted from the measured signal, and the circular dichroism of the sample is proportional to $I(1f)/I(DC)$.

Similar to the previous derivation, we can write out the Jones matrix for circular dichroism. The output light after going through a 45 degree polarizer, PEM and sample is,

$$O = M \cdot S(\theta) \cdot PEM \cdot P(45) \cdot \begin{bmatrix} E \\ 0 \end{bmatrix}$$
$$= E \begin{bmatrix} -\frac{\Delta \sin(\theta)^2}{2} - \frac{e^{\tau i}\left(c - \frac{\Delta \sin(2\theta)}{2} \right)}{2} + \frac{1}{2} \\ -\frac{c}{2} + \frac{e^{\tau i}\left(\Delta \cos(\theta)^2 - 1 \right)}{2} - \frac{\Delta \sin(2\theta)}{4} \end{bmatrix}$$

The intensity measured by the photo detector is,

$$I(t) = E^2\left(\sin(\tau)\eta + \cos(\tau)\frac{\delta \sin(2\theta)}{2} - \frac{\delta}{2} + \frac{1}{2} \right)$$
$$+ \mathcal{O}(h)$$
$$= E^2\left[\frac{1}{2} - \frac{\delta}{2} + 2J_1(\tau_0)\sin(\omega t)\eta \right.$$
$$\left. + \left(J_0(\tau_0) + 2J_2(\tau_0)\cos(2\omega t) \right)\frac{\delta \sin(2\theta)}{2} \right]$$
$$+ \mathcal{O}(h)$$

where $\tau_0 = \frac{\pi}{2}$. For circular dichroism I_{CD}, we are measuring the ratio between the $1f$ and the DC component which is equal to,

$$I_{CD} = \frac{I_{lock}(1f)}{I_{lock}(DC)} = 2\sqrt{2}J_1(\frac{\pi}{2})\eta \quad (7)$$

We see from Eq. (7) that the circular dichroism signal does not depend on the sample orientation (θ) as expected, and is only related to the ellipticity η term from the MOKE effect.

In our optical setup, we used a 50:50 non-polarizing cube in between the PEM and objective to collect the signal. The non-polarizing cube has different transmission coefficients for the s and p polarized light across the 750 - 850 nm wavelength range of our pulsed laser. To account for the this s and p transmission differences and rule out its effect on the circular dichroism signal, we can add in the Jones matrix for the cube C into the CD derivation,

$$C = \begin{bmatrix} \sqrt{T_p} & 0 \\ 0 & \sqrt{T_s} \end{bmatrix}$$

where T_s and T_p are the transmission coefficient for the s and p polarized light. The output light in this case is,

$$O = \begin{bmatrix} \sqrt{1-T_p} & 0 \\ 0 & \sqrt{1-T_s} \end{bmatrix} \cdot M \cdot S(\theta) \cdot \begin{bmatrix} \sqrt{T_p} & 0 \\ 0 & \sqrt{T_s} \end{bmatrix}$$
$$\cdot PEM \cdot P(45) \cdot \begin{bmatrix} E \\ 0 \end{bmatrix}$$

The intensity measured by the photo detector is,

$$I(t) = -2J_1(\tau_0)\sin(\omega t)\sqrt{T_p T_s}\left[\frac{(T_s + T_p - 2)\eta}{2}\right.$$
$$\left. + \frac{(T_s - T_p)\kappa\sin(2\theta)}{4}\right] - \left(J_0(\tau_0) + 2J_2(\tau_0)\cos(\omega t)\right)$$
$$\sqrt{T_p T_s}\left[\frac{(T_s - T_p)\theta_K}{2} + \frac{(T_p + T_s - 2)\delta\sin(2\theta)}{4}\right]$$
$$+ \frac{T_s + T_p - T_s^2 - T_p^2}{4} + \frac{\delta}{2}\left[T_s^2 - T_s + T_s\sin^2(\theta)\right.$$
$$\left. - T_p\sin^2(\theta) - T_s^2\sin^2(\theta) + T_p^2\sin(\theta)\right] + \mathcal{O}(h)$$

where $\eta_0 = \frac{\pi}{2}$. Now, the circular dichroism signal becomes,

$$I_{CD} = \frac{I_{lock}(1f)}{I_{lock}(DC)} = \frac{J_1(\tau_0)\sqrt{2T_p T_s}}{T_s + T_p - T_s^2 - T_p^2}$$
$$\left[2(T_s + T_p - 2)\eta + (T_s - T_p)\kappa\sin(2\theta)\right]$$

We see now there is a birefringence correction term in the circular dichroism signal as follows,

$$I_{bire} = \frac{J_1(\eta_0)\sqrt{2T_p T_s}(T_s - T_p)\kappa\sin(2\theta)}{T_s + T_p - T_s^2 - T_p^2} \qquad (8)$$

This correction term is proportional to the product of κ and the difference in the transmission coefficients $T_s - T_p$. Given the specification of the non-polarized cube $|T_s - T_p| \sim 10^{-2}$, we can estimate the magnitude of such correction to be,

$$I_{bire} \propto \kappa \cdot (T_s - T_p) = 10^{-4} \cdot 10^{-2} = 10^{-6} \qquad (9)$$

The birefringence correction is one order of magnitude less than the circular dichroism signal of the samples, thus can be ignored in our measurement.

D. CD Theory

We derive the general CD effect and discuss consequences of TRS-breaking and crystal-symmetry-breaking on CD. According to Fermi's golden rule, the absorption rate of circular light with helicity $\sigma_\pm$ is

$$I(\sigma_\pm) = \frac{2\pi}{\hbar}\sum_{c,v}|\langle c|H'|v\rangle|^2\delta(E_c - E_v - \hbar\omega), \qquad (10)$$

where v and c refer to valance and conduction band states, respectively, and $\hbar\omega$ is the photon energy. H' is the interaction Hamiltonian, whose expression is given by

$$H' = -e\boldsymbol{E}\cdot\boldsymbol{r} - \boldsymbol{m}\cdot\boldsymbol{B}. \qquad (11)$$

The two terms on the right-hand side of Eq. (11) correspond to electric and magnetic dipole interactions, respectively. The magnetic dipole term is usually much weaker than the electric dipole term. However, the magnetic dipole cannot be ignored for CD in time-reversal invariant systems where the electric dipole contribution vanishes as illustrated following.

For helical photon $\sigma_\pm$, the electric and magnetic field is

$$\boldsymbol{E} = E_0(1, \pm i, 0) \quad , \quad \boldsymbol{B} = \frac{E_0}{c}(\mp i, 1, 0), \qquad (12)$$

so that the interaction matrix element is

$$|\langle c|H'_\pm|v\rangle|^2 = |E_0|^2\left|\left\langle c\left|er_\pm \mp i\frac{m_\pm}{c}\right|v\right\rangle\right|^2 \qquad (13)$$

where $r_\pm = x \pm iy$, and $m_\pm = m_x \pm im_y$. Therefore the CD is

$$I(\sigma_+) - I(\sigma_-) \propto |\langle c|H'_+|v\rangle|^2 - |\langle c|H'_-|v\rangle|^2$$
$$= 2\text{Im}\left[\underbrace{e^2\langle v|x|c\rangle\langle c|y|v\rangle}_{①}\right.$$
$$+ \underbrace{\frac{e}{c}\langle v|m_x|c\rangle\langle c|x|v\rangle + \frac{e}{c}\langle v|m_y|c\rangle\langle c|y|v\rangle}_{②} \qquad (14)$$
$$\left. + \underbrace{\frac{1}{c^2}\langle v|m_y|c\rangle\langle c|m_x|v\rangle}_{③}\right].$$

In Eq. (14), ① comes from electric dipole, ② originates in both electric and magnetic dipoles, and ③ come from merely magnetic dipole interactions. The ③ term is usually ignored since it is to small compared to ① and ②.

① is the Berry curvature between valance band v and conduction band c. It is even under inversion symmetry but odd under TRS. It is usually called magnetic CD in literature. ② is even under TRS but odd for mirror or inversion, because, for example, $\langle v|m_x|c\rangle\langle c|x|v\rangle$ is odd under $x/y \to -x/-y$ reflection or $(x, y, z) \to (-x, -y, -z)$ inversion. Therefore, if TRS is broken, both ① and ② are nonzero. If TRS is conserved, only ② can appear in a chiral material. If both TRS and inversion symmetry exist, the CD effect vanishes. In the case of inversion and/or mirror symmetries in the material, the CD effect due to ① indicates the TRS-breaking.

II. ACKNOWLEDGEMENT

III.   AUTHOR CONTRIBUTION

L.W. conceived and supervised the project. Y.X. performed the experiments and analyzed the data with Z.N. and L.W.. Y.L. and B.Y. performed the CD symmetry analysis. B.O. and S.W. grew the crystals. L.W.,Y.X., S.W., B.Y., and L.B. discussed and interpreted the data. L.W. and Y.X. wrote the manuscript from input of all authors. All authors edited the manuscript.